

www.acsami.org Research Article

Two Birds with One Stone: Prelithiated Two-Dimensional Nanohybrids as High-Performance Anode Materials for Lithium-Ion Batteries

Sichen Wei, Yu Fu, Pinku Roy, Xiao Tong, Hongyan Yue, Maomao Liu, Hemendra Nath Jaiswal, Simran Shahi, Yannick Iniatius Gata, Tony Butler, Huamin Li,* Quanxi Jia, and Fei Yao*



Cite This: ACS Appl. Mater. Interfaces 2022, 14, 35673-35681



ACCESS

Metrics & More

Article Recommendations

Supporting Information

MoS₂/MXene

FFFFFFFF

IT Phase
Ratio
50%

Deep phase
transition

To Supporting Information

The Properties of the Pro

ABSTRACT: As an inexpensive and naturally abundant two-dimensional (2D) material, molybdenum disulfide (MoS_2) exhibits a high Li-ion storage capacity along with a low volume expansion upon lithiation, rendering it an alternative anode material for lithium-ion batteries (LIBs). However, the challenge of using MoS_2 -based anodes is their intrinsically low electrical conductivity and unsatisfied cycle stability. To address the above issues, we have exploited a wet chemical technique and integrated MoS_2 with highly conductive titanium carbide (Ti_3C_2) MXene to form a 2D nanohybrid. The binary hybrids were then subjected to an n-butyllithium (n-Buli) treatment to induce both MoS_2 deep phase transition and MXene surface functionality modulation simultaneously. We observed a substantial increase in 1T-phase MoS_2 content and a clear suppression of -F-containing functional groups in MXene due to the prelithiation process enabled by the n-Buli treatment. Such an approach not only increases the overall network conductivity but also improves Li-ion diffusion kinetics. As a result, the MoS_2/Ti_3C_2 composite with n-Buli treatment delivered a high Li-ion storage capacity (540 mA h g⁻¹ at 100 mA g⁻¹), outstanding cycle stability (up to 300 cycles), and excellent rate capability. This work provides an effective strategy for the structure—property engineering of 2D materials and sheds light on the rational design of high-performance LIBs using 2D-based anode materials.

KEYWORDS: two-dimensional composite, molybdenum disulfide, MXene, Li-ion battery, prelithiation

■ INTRODUCTION

It is estimated that CO2 emissions must be reduced by at least 50% to limit global warming to 2 °C by 2050^{1,2} in order to avoid a future in which everyday life around the world is marked by its worst and the most devastating effect—climate change. The pressing need for carbon emission reduction calls for a rapid move toward electrified mobility and expanded deployment of solar and wind on electric grids. As a result, high-performance electrical energy storage systems are highly demanded. Rechargeable lithium-ion batteries (LIBs) are the most widely used battery system in portable electronics and electric vehicles nowadays because of their high energy per unit mass, power-to-weight ratio, high-temperature performance, and low self-discharge. 1-5 Nevertheless, conventional graphite anodes exhibit a rather small theoretical maximum Li storage capacity (372 mA h g⁻¹), 1,6 which is far from satisfaction for the development of modern society. As a result, extensive research has been conducted on various high-specific-capacity anode materials, such as nanostructured carbon, ⁷⁻⁹ silicon, ¹⁰⁻¹² metal oxides, ¹³⁻¹⁶ and two-dimensional (2D) layered transition metal dichalcogenides (TMDs),^{17–19} to further improve the performance of LIBs.

As a representative TMD, molybdenum disulfide (MoS₂) provides a highly competitive landscape in terms of electrochemical performance when employed as a LIB anode. Compared to the conventional graphite anode, MoS₂ exhibits three and a half times higher capacity (up to 1290 mA h g⁻¹) and an improved safety benefiting from less dendrite formation associated with an intermediate lithiation voltage (1.1–2 V vs Li/Li⁺). In addition, it shows a lower degree of volume expansion (103%) upon lithiation compared to Si (280% for Li₁₅Si₄ stoichiometry) with a better rate capability and capacity retention. ^{12,17} However, the intrinsically low electrical

Received: May 5, 2022 Accepted: July 14, 2022 Published: August 1, 2022





conductivity arising from the semiconducting nature of the 2H phase has been a limiting factor for achieving a high-performance MoS₂-based anode.

Tremendous efforts have been devoted to improve the conductivity of 2H-MoS₂, where phase engineering and composite formation are now at the center of these efforts. MoS₂ phase transition from the semiconducting 2H phase to the metallic 1T phase can be achieved through ion intercalation, doping engineering, strain application, 20-24 and so forth. Among the abovementioned strategies, solutionphase-based ion intercalation achieved during the MoS₂ solvothermal synthesis process has been considered as one of the most effective approaches because of its simplicity, low cost, scalability, and operational stability. Recently, we successfully employed a one-step solvothermal method in a bisolvent medium for dual-phase MoS2 synthesis and demonstrated excellent electrochemical catalytic performance.²⁵ Nevertheless, the 1T-phase content in the obtained MoS₂ structure is relatively low, which could potentially limit the anode performance.

On the other hand, integrating MoS₂ with highly conductive frameworks to form hybrid composites is another effective approach to improve its conductivity. Compared with a widely used carbonaceous framework such as graphene, 18,26-3 MXenes, a group of 2D materials consisting of transition metal carbides/nitrides/carbonitrides, exhibit enriched material chemistry, relatively high electrical conductivity, and superior hydrophilicity, rendering them an attractive alternative as the conductive frameworks. 35-37 In contrast to the charge-neutral graphene, MXenes exhibit a negatively charged surface due to the existence of rich surface functional groups, such as -OH, -O, and -F, which not only enhance the dispersion of precursors but also promote the MoS₂ nucleation in the solvent, making MXenes a superior substrate candidate for the synthesis of MoS₂. 38 Moreover, it has been reported that the MXene electrochemical properties strongly depended on the nature of surface terminal groups, which endow MXenes with an extra degree of freedom for the LIB performance optimization. For instance, the -F-containing functional groups with a higher Li-ion diffusion barrier would impede the ion transport and decrease the capacity, highlighting the necessity of surface functionality modulation. 39,40

Recently, Ti₃C₂ MXene, one of the representative MXenes, has been composited with MoS2 for LIB applications. For instance, Du et al.41 synthesized MoS2 nanoflakes and Ti3C2 hybrid structures by a hydrothermal method and reported a reversible discharge capacity of 614 mA h $\rm g^{-1}$ at 0.1 A $\rm g^{-1}$ after 70 cycles. Zheng et al. 42 intercalated MoS $_2$ nanosheets into partially oxidized Ti₃C₂ and demonstrated a discharge capacity of 230 mA h g⁻¹ at 0.5 A g⁻¹ for 50 cycles. Shen et al.⁴³ produced the MoS_2 -decorated Ti_3C_2 using a solid-phase sintering method and achieved 131.6 mA h g⁻¹ at 1 A g⁻¹ for 200 cycles. The aforementioned reports mostly ascribed the improved anode performance of hybrid structures to the enlarged interlayer spacing after the composite integration and the inherent high conductivity of MXene compared with that of the single-component anode. The impacts of MoS₂ phase engineering together with MXene surface functionality modulation on LIB performance, however, have never been investigated, hindering the fundamental understanding and performance improvement of the nanocomposite.

Herein, we aim to design and conduct an experiment to trigger a deep phase transition of MoS₂ and engineer the

surface functionality of MXene simultaneously. We employed the dual-phase MoS_2 and Ti_3C_2 MXene hybrid obtained from the solvothermal method as starting materials and performed an n-butyllithium (n-Buli) solution treatment to prelithiate the nanocomposites. We observed a substantial increase in 1T-phase content of MoS_2 from 50 to 75% and a clear suppression of -F-containing functional groups on the MXene surface due to the lithium-ion intercalation, leading to a clear improvement of the overall network conductivity and Li-ion diffusion kinetics. As a result, the n-Buli-treated MoS_2/Ti_3C_2 hybrid exhibits a reversible Li-ion storage capacity of \sim 540 mA h g $^{-1}$ for 300 cycles at 100 mA g $^{-1}$ with a clearly improved rate capability compared with that of the pristine nanohybrid.

METHODS

Materials. Anhydrous ethanol, lithium fluoride (LiF), hydrochloric acid (HCl), ammonium molybdate, thiourea and N,N-dimethylformamide (DMF), n-Buli in hexane solution, hexane, and N-methyl-2-pyrrolidone (NMP) were purchased from Fisher Scientific, USA. ${\rm Ti}_3{\rm AlC}_2$ was purchased from Beijing Forsman Scientific Co. Ltd., China. Super P and polyvinylidene fluoride (PVDF) were purchased from AOT Electronics Technology Co., LTD, China. All chemicals were used as received without any further purification.

Preparation of Ti₃C₂ MXene. The Ti_3C_2 was prepared by the in situ HF etching method. As Specifically, 2 g of LiF powder was slowly added into 40 mL of HCl (9 M) solution and stirred for 30 min until LiF was fully dissolved. 2 g of Ti_3AlC_2 was slowly added into the LiF/HCl mixture, which was placed in an ice bath subsequently. The solution was kept at 40 °C for 48 h with continuous stirring. After the reaction, the black powder was collected by centrifugation and washed with deionized (DI) water until the supernatant reached a pH value larger than 6. The powder was dried under vacuum at 60 °C for 12 h.

Synthesis of the Dual-Phase MoS_2/Ti_3C_2 Composite. 1 g of the as-prepared Ti_3C_2 powder was added into 60 mL of DI water/DMF bisolvent, followed by ultrasonication to form a homogenous suspension. 1.928 g of ammonium molybdate and 3.645 g of thiourea were slowly added into the suspension and stirred until the precursors were well-mixed. The suspension was then transferred into a 100 mL Teflon-lined autoclave and kept at 195 °C for 22 h. After naturally cooling down to room temperature, the product was collected by centrifugation and washed with DI water and ethanol at least five times, followed by vacuum drying at 60 °C for overnight. The asprepared composite is denoted as p-MT.

Preparation of *n***-Buli-Treated MoS**₂/Ti₃C₂**.** 0.5 g of p-MT was dried in a vacuum oven at 100 °C for overnight in order to remove the moisture in the powder. The dried powder was then transferred into an Ar-filled glovebox ($O_2 < 0.01$ ppm and $H_2O < 0.01$ ppm). 10 mL of *n*-Buli/hexane solution was slowly added to the powder in order to avoid vigorous reaction, and the sample was kept in the glovebox for 15 days to allow a thorough reaction to occur. The *n*-Buli-treated sample is denoted as n-MT. After the reaction, the n-MT was first washed with hexane five times inside the glovebox to remove excessive *n*-Buli, and then, the product was extracted from the glovebox and washed with DI water by vacuum filtration to wash out the residual hexane. In the end, the sample was dried in a vacuum oven overnight.

Characterization. X-ray diffraction (XRD) was performed using a Rigaku Ultima IV system with Cu K α radiation (wavelength = 0.154 nm). Raman spectra were collected using Renishaw InVia with an excitation laser wavelength of 514 nm. The morphologies of all products were investigated by field-emission scanning electron microscopy [FE-SEM, Carl Zeiss AURIGA CrossBeam] with an Oxford energy dispersive X-ray spectroscopy (EDS) system. X-ray photoelectron spectroscopy (XPS) was performed using a monochromatic Al K α source ($h\nu$ = 1486.6 eV) (ESCALAB 250, Thermo Scientific).

Electrochemical Measurements. The LIB electrode performance was evaluated in a half-cell configuration in a type CR2032 coin cell. The coin cell was fabricated in an Ar-filled glovebox ($O_2 < 0.01$ ppm and H₂O < 0.01 ppm) with n-MT or p-MT as working electrodes, LiPF₆ in EC/DMC as the electrolyte, and Li foil as the counter/reference electrode, respectively. The working electrode was prepared by mixing the nanocomposite, Super P, and PVDF in a weight ratio of 8: 1: 1 in NMP and then doctor-bladed on a Cu current collector followed by drying in a vacuum oven. Galvanostatic charge-discharge (GCD) and cyclic voltammetry (CV) were tested in the potential range of 0-3 V versus Li/Li+ with a current density and scan rate of 0.1 A/g and 0.05 mV/s, respectively. The electrochemical impedance spectroscopy (EIS) was performed at open-circuit potential in the frequency range of 10 mHz to 100 kHz with the amplitude of 5 mV. All the electrochemical tests were performed on a Biologic VMP3 potentiostat at room temperature.

RESULTS AND DISCUSSION

As shown in the top panel in Figure 1, the p-MT composite was synthesized using a bisolvent solvothermal method



Figure 1. Schematic illustration of n-Buli treatment for MoS_2/MX ene nanohybrid structures.

reported previously.²⁵ Briefly, accordion-like Ti₃C₂ MXene flakes were produced by the in situ HF etching method.⁴⁴ Specifically, the reaction between HCl and LiF will in situ produce HF, which can effectively etch off the Al layer from the Ti₃AlC₂ precursor by breaking the relatively weak Ti–Al bond compared to the Ti–C bond.^{36,37} The obtained Ti₃C₂ flakes were then added into DI water/DMF bisolvent together

with ammonium molybdate and thiourea powders, which served as Mo and S sources, respectively. Our previous work demonstrated that the use of bisolvent not only induces the phase transition of MoS₂ from the semiconducting 2H to metallic 1T phase by NH₄+-ion intercalation but also prevents the undesired oxidation of MXene, leading to the improvement of conductivity and stability of the hybrid structure simultaneously. $^{45-47}$ The as-prepared p-MT sample was then soaked into n-Buli/hexane solution for 15 days in a glovebox to obtain the n-MT sample. As an organolithium reagent, n-Buli has been widely used as an intercalating agent for 2D materials exfoliation. 20,48 We anticipate that the *n*-Buli treatment can further improve the composite electrochemical performance in the following aspects (see the bottom panels in Figure 1): (i) increase the conductivity of MoS2 by Li-ion interaction to trigger deep phase transition of MoS2 and (ii) reduce the content of F-containing functional groups, which are known for adversely affecting the battery performance.⁴⁹

To investigate the structure and composition of the products, a series of characterizations were conducted. The SEM and transmission electron microscopy (TEM) images of p-MT are shown in Figure 2a,b, where MoS₂ flakes were found uniformly wrapped around the Ti₃C₂ layers. The interlayer distance of MoS2 and Ti3C2 in p-MT is extracted from highresolution TEM (HRTEM) images (Figure 2c,d), and the values are 0.98 and 1.36 nm, respectively. These values are found to be larger than the reported values for pure 2H phase MoS₂ (0.64 nm) obtained from an in situ sulfurization method 46,47,50 and Ti_3C_2 flakes (1 nm) from typical HF technique. 47,51 The increased interlayer space can be ascribed to the NH₄⁺-ion intercalation during the solvothermal synthesis process and the integrated stacking nature of the 2D layers, which will be beneficial for facile ion transport during battery operation.

The SEM and TEM images of n-MT are shown in Figure 2e and f, where distinct, largely expanded features are observed. We suspect that the severe structure evolution after *n*-Buli treatment is related to the H₂ gas generation along with heat production originating from the vigorous reaction between *n*-Buli and the small amount of residual water trapped within the 2D composite.²⁰ Additional SEM images of n-MT can be found in Figure S1. The HRTEM images of n-MT are shown in Figure 2g,h, and the interlayer distance of MoS₂ and Ti₃C₂

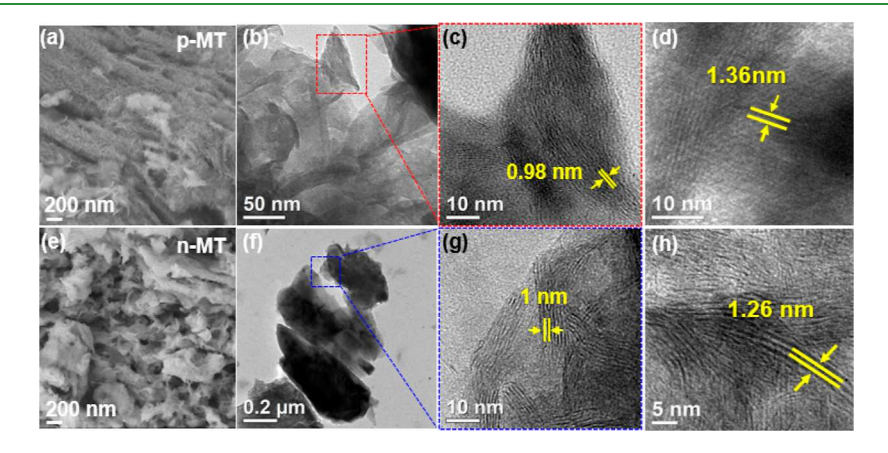


Figure 2. SEM (a) and TEM (b) images of the p-MT sample. HRTEM images of p-MT with the marked interlayer distances of MoS_2 flakes (c) and MXene sheets (d). (e,f) SEM and TEM images of the n-MT nanohybrid. The interlayer distances of MoS_2 and MXene are shown in (g,h), respectively.

MXene was extracted to be 1 and 1.26 nm, respectively. The interlayer distance of MoS₂ is almost unchanged compared to the one in p-MT but decreased in the case of Ti₃C₂ MXene after *n*-Buli treatment (see more HRTEM images in Figure S2, and a detailed discussion can be found in the following section). The EDS mappings can be found in Figure S3 with uniformly distributed MoS₂ and MXene-related elements, suggesting the existence of MoS2 and Ti3C2 MXene components in the composite before and after n-Buli treatment. The presence of oxygen species can be attributed to the presence of oxygen functional groups in MXene along with the unavoidable sample oxidation. A low -F content was detected in both p-MT and n-MT. However, the atomic ratio of the -F content was clearly reduced in n-MT (0.3%) compared to that of p-MT (11.1%) after the *n*-Buli treatment, which is expected to reduce the diffusion barrier of Li ions and therefore improve the rate performance of the battery anode.

Figure 3a shows the Raman spectra of p-MT and n-MT. Clear E_{1g} (280 cm⁻¹), E_{2g} (377 cm⁻¹), and A_{1g} (404 cm⁻¹)

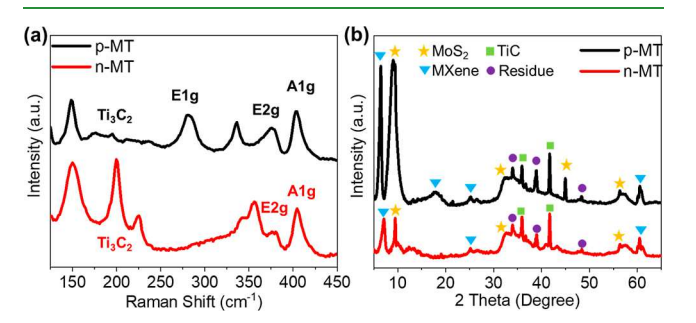


Figure 3. Raman spectra (a) and XRD patterns (b) of pristine and *n*-Buli-treated MoS₂/MXene hybrid structures.

peaks corresponding to the vibration of atoms along in-plane (E_{1g}, E_{2g}) and out-of-plane (A_{1g}) directions have been detected in p-MT and are in good agreement with the previous reported 2H-phase MoS_2 . In addition, the observation of the vibration peaks at 151 and 336 cm⁻¹ suggests a clear 1T phase

in p-MT. The formation of the 1T phase is triggered by the $\mathrm{NH_4^+}$ -ion intercalation introduced during the bisolvent synthesis process, where both ammonium molybdate and DMF act as the abundant source of $\mathrm{NH_4^+}$ ions. Specifically, the intercalated $\mathrm{NH_4^+}$ can stimulate the charge imbalance between $\mathrm{Mo^{3+}}$ and $\mathrm{Mo^{4+}}$ and cause the S plane sliding and therefore the $\mathrm{MoS_2}$ crystal structure distortion, resulting in the phase transformation from 2H to 1T eventually. S4

In the case of n-MT, four 1T phase-related peaks located at 150, 225.6, 340, and 356 cm⁻¹ corresponding to the previously reported Li intercalated ${\rm MoS_2}^{55}$ are well-observed. It is worth mentioning that the intensities of both ${\rm A_{1g}}$ and ${\rm E_{2g}}$ peaks are reduced in n-MT compared with p-MT, indicating a less content of the 2H phase in n-MT. Furthermore, we noticed that the ${\rm E_{1g}}$ mode was not detectable in n-MT, which can be ascribed to the swollen and enlarged ${\rm MoS_2}$ features after Li intercalation, inducing a relatively less amount of edge plane exposure under the laser spot. Si In addition, it can be seen that a peak at 225.6 cm⁻¹ emerged in n-MT due to the structure distortion along with potential defect generation after n-Buli treatment. The enhanced peak at 200 cm⁻¹ can be attributed to the increased exposure of ${\rm Ti_3C_2}$ MXene layers resulting from the microstructure evolution of ${\rm MoS_2}$ after n-Buli treatment, where sparser ${\rm MoS_2}$ layers were observed.

The XRD pattern of both samples can be found in Figure 3b. The diffraction pattern of p-MT shows obvious diffraction peaks at 6.47, 17.8, 25.27, and 60.47°, which can be correlated to the Ti₃C₂ MXene (002), (006), (008), and (110) planes, respectively. The MoS₂-related diffraction peaks at 9.2, 32.3, 44.6, and 56.9° were clearly observed, corresponding to the (002), (100), (006), and (110) planes, respectively. Two peaks located at 35.9 and 41.7° are attributed to TiC, which is originally from the Ti₃AlC₂ precursor. ^{57,58} Additional weak peaks (marked with purple dots) were also observed from both samples, which can be ascribed to the Al-related residue from the wet chemical etching process. The interlayer spacing of Ti₃C₂ and MoS₂ was calculated via Bragg's diffraction equation, and the values are 1.36 and 0.96 nm, respectively,

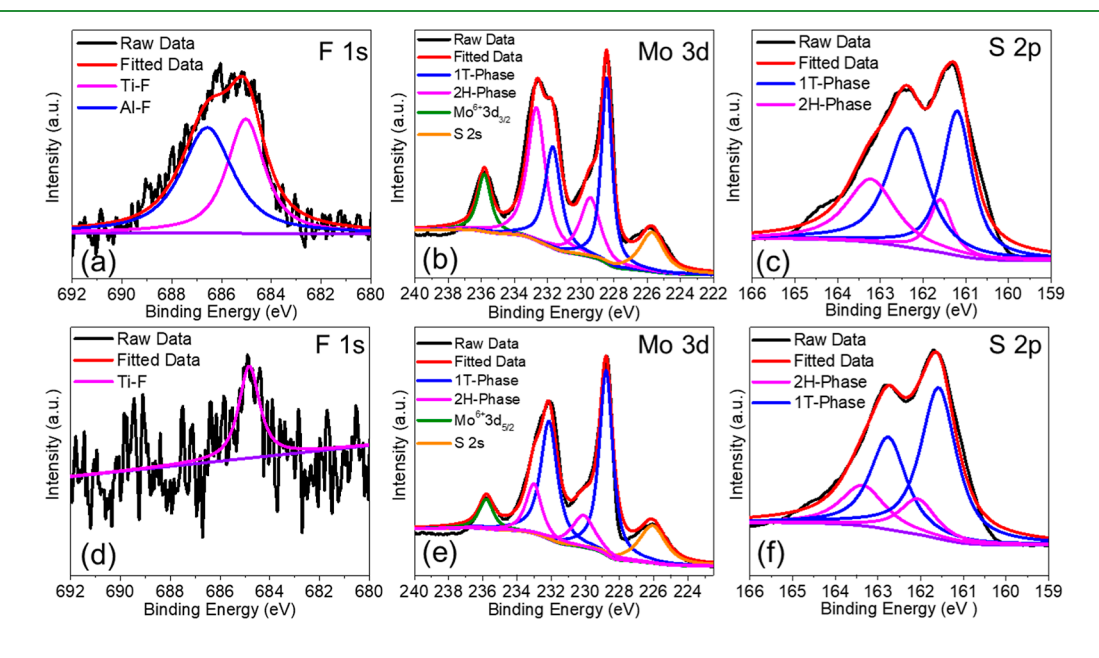


Figure 4. Deconvoluted XPS spectra of p-MT (top panel) and n-MT (bottom panel), showing the binding energy of fluorine (a,d), molybdenum (b,e), and sulfur (c,f).

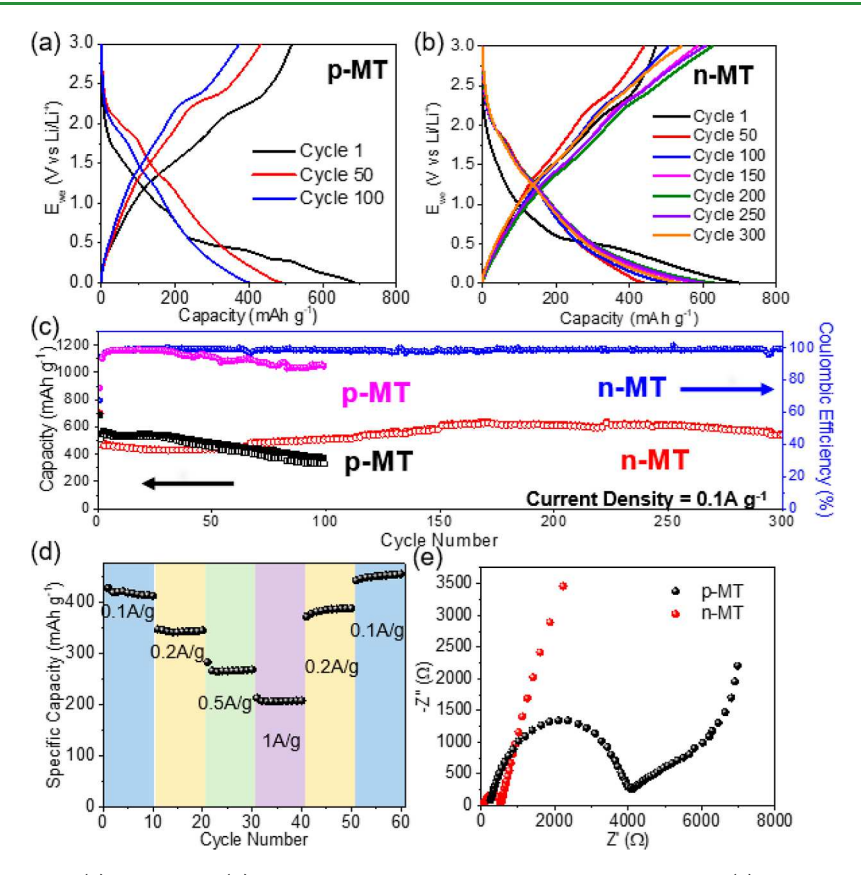


Figure 5. GCD profiles of p-MT (a) and n-MT (b). The cycling performance of the 2D nanohybrids (c). Rate performance of n-MT (d) and Nyquist plot of the 2D hybrids (e).

which are in line with the HRTEM results shown in Figure 2c,d. In the case of n-MT, clear peak intensity reduction and the disappearance of (006) plane-related peaks in both MXene and MoS_2 can be observed, indicating a decreased structural crystallinity after n-Buli treatment. This result is also in agreement with the 225.6 cm $^{-1}$ Raman peak emergence in n-MT (Figure 3a), which was attributed to the higher defect density in MoS_2 after lithiation. The amorphous ring features shown in the selected area electron diffraction (SAED) pattern (see Figure S4) also suggest a poor crystallinity resulting from the intercalation of NH_4^+ and/or Li^+ ions. 59,60 The amorphous nature of the binary composites is beneficial for the MoS_2 -based anode performance due to the increased ion intercalation sites and reduced ion diffusion resistance. 60,61

It is worth mentioning that although the MoS₂(002) peak does not show a clear change in n-MT, the Ti₃C₂(002) peak upshifts to 7.12° corresponding to a reduced interlayer spacing of 1.26 nm compared with p-MT, which echoes well with the TEM result shown in Figures 2 and S2. In the case of MoS_2 , the interlayer distance remained similar after n-Buli treatment, which can be understood since sufficient interlayer expansion has been achieved via NH4+-ion intercalation during the bisolvent synthesis process. In the case of MXene, the reduction of interlayer distance upon lithiation⁶² can be ascribed to the moisture loss⁶³ and electrostatic interactions between the inserted Li ions and the inherently negatively charged MXene layers. In addition, the de-functionalization of the F-containing group in the MXene layers could also contribute to the interlayer space reduction (see discussion in the section below).

XPS was performed to provide further insight into the chemical constitution and phase information. The complete survey of p-MT and n-MT is shown in Figure S5a,b, respectively. A small peak located at ~685 eV corresponding to the F 1s signal was detected in p-MT, whereas there was no obvious peak observed in the range of 600-800 eV for n-MT. The deconvoluted F 1s spectra for both samples are shown in Figure 4a,d. The peak in p-MT is clear and can be deconvoluted into Ti-F and Al-F related bonds, originating from the incomplete etching of the Al layer in the Ti₃AlC₂ phase using LiF. However, only a tiny Ti-F bond-related signal was observed in n-MT, suggesting the effective removal of F-containing functional groups from the Ti₃C₂ MXene after n-Buli treatment, which corresponds well to the observation in Figure S3. The reduction of F-containing functional groups can be attributed to the Ti-F bond weakening and cleavage upon Li⁺-ion intercalation^{64,65} during the *n*-Buli treatment.

To investigate the MoS₂ phase transition in these two samples, the Mo 3d spectra were deconvoluted, and the related results are shown in Figure 4b,e. In p-MT (see Figure 4b), two sets of peak doublets located at 229.5/232.7 eV and 228.5/231.7 eV were observed, which can be assigned to the 2H (pink line) and 1T phases (blue line) of MoS₂, respectively.⁶⁶ A similar analysis was carried out for the n-MT sample, and the 1T phase ratio was calculated according to the area of the peaks. The result shows that n-MT exhibits a higher 1T phase ratio (75%) compared to p-MT (50%). Figure 4c,f exhibits the deconvoluted S 2p spectra of the two samples where two sets of peak doublets at 162.1/163.4 eV and 161.6/162.75 eV are observed, corresponding to the 2H (pink line) and 1T phases (blue line), respectively, and a higher 1T phase ratio of 74%

was also detected in n-MT. The above results demonstrate that a deeper phase transition of MoS2 and surface functionality modulation of MXene has been successfully achieved by the n-Buli treatment, which is expected to improve the anode performance in terms of stability and rate capability because of the improved conductivity and facile Li⁺ diffusion in the hybrid associated with the increased amount of the 1T metallic MoS₂ phase along with a higher population of defective sites and the reduced amount of F-containing functional groups, which has a higher Li⁺ diffusion barrier in MXene.

The electrochemical battery performance for both samples was evaluated by GCD at a current density of 0.1 A g⁻¹ in the potential window of 0.01-3 V (vs Li/Li⁺). Figure 5a displays the GCD curves of p-MT. In the first lithiation process, the plateaus observed at $\sim\!1$ and 0.5 V are associated with the Liion intercalation into MoS₂, forming Li_xMoS₂ (see equation 1) with the phase transformation from 2H to 1T and its further lithiation to form Mo nanoparticles embedded in Li₂S matrix (see eq 2). In the first delithiation process, two plateaus at 1.5 and 2.2 V are correlated to the oxidation of Mo to MoS_2 (eq 3) and the transformation of Li₂S into S (eq 4), respectively. In the following charge/discharge cycles, two sets of plateaus can be identified. The plateaus at 1.86 V (discharge)/2.25 V (charge) and 1.3 V (discharge)/1.6 V (charge) can be assigned to the redox couples of S/Li₂S and MoS₂/Mo (eqs 3 and 4), respectively. The p-MT nanocomposite delivers a high initial lithiation capacity of 687 mA h g^{-1} followed by a delithiation capacity of ~516 mA h g^{-1} in the first cycle. The large irreversible capacity can be attributed to solid–electrolyte interphase formation, which could originate from electrolyte decomposition. At the 100th charge/discharge cycle, a delithiation capacity of 330 mA h g⁻¹ is observed.

$$MoS_2 + xLi^+ + xe^- \rightarrow Li_x MoS_2$$
 (1)

$$\text{Li}_x \text{MoS}_2 + 4(1-x)\text{Li}^+ + (4-x)e^- \to \text{Mo} + 2\text{Li}_2 \text{S}$$
(2)

$$Mo + 2Li2S \leq MoS2 + LixMoS2 + 4Li+ + 4e-$$
 (3)

$$2Li_2S \leftrightarrows 2S + 4Li^+ + 4e^- \tag{4}$$

In the case of n-MT (Figure 5b), two distinct features in charge/discharge profiles can be observed in contrast to p-MT. First, the absence of the plateau at ~1 V can be explained as the pre-existence of Li_xMoS₂ in n-MT induced by the *n*-Buli treatment. This observation also suggests a high 1T phase content in n-MT, which is in line with our observation in Figure 4. Second, despite general plateau formations associated with Li_xMoS₂ decomposition and reversible reactions between S/Li_2S and MoS_2/Mo can be identified (eqs 2-4), the plateaus are not as obvious as those in p-MT due to the severe layered structure deformation after the n-Buli treatment (see Figure 2e). 67 The CV curves of the hybrid 2D composites can be found in Figure S6. In the case of p-MT, all the peaks correspond well with the plateaus (1.86 V/2.25 V and 1.3 V/ 1.6 V) observed in the GCD curve (see Figure 5a). In the case of n-MT, a broad peak located at 0.5 V emerged, which is due to the decomposition of Li_xMoS₂ induced by the prelithiation during n-Buli treatment. The n-MT nanohybrids delivered a similar initial lithiation capacity to that of p-MT (~701 mA h g⁻¹) but showed a minor decrease up to the 50th cycle and then increased to a higher capacity in the following cycles. For instance, the delithiation capacities at the 100th and 200th

cycles were found to be \sim 508 and 610 mA h g⁻¹, respectively. The slow increase in the capacity can be attributed to the activation process of the electrode material upon cycling, which gradually generates micro-channels for electrolyte ion transport and therefore effectively enhance the Li-ion intercalation/extraction efficiency.⁶⁸ Eventually, the n-MT composite maintained a delithiation capacity of 540 mA h g⁻¹ at the 300th cycle, demonstrating superior Li-ion storage capacity compared to that of p-MT and pure MoS₂ or Ti₃C₂ MXene samples (see Table S1).

Figure 5c shows the comparison of the cycling stability of p-MT and n-MT composites at a constant current density of 100 mA g⁻¹. The Coulombic efficiency (CE) of p-MT and n-MT at the beginning of the cycling is 75 and 67%, respectively. In the following cycles, the CE of the p-MT anode decreases to 88% at the 100th cycle along with severe capacity fading. In sharp contrast, the n-MT nanocomposite shows a much more stable cycling performance with a stable CE of 99.6% up to the 300th cycle. The superior cycling performance of the n-MT hybrid electrode is closely related to its better electrical conductivity arising from a higher 1T phase MoS₂ content and a reduction of the F-content in the nanohybrids, benefiting from the *n*-Buli treatment. In addition, the prelithiation process of n-MT nanohybrids could compensate for the active lithium losses in the subsequential cycles, which is also beneficial for the anode stability. Figure 5d shows the rate capability of the n-MT composites. The hybrid electrode presents an excellent rate capability with the reversible capacities of 430, 350, 268, and 214 mA h g⁻¹ at different current densities of 0.1, 0.2, 0.5, and 1 A g⁻¹, respectively, which is obviously more stable than p-MT (see Figure S7). When the current density returns to 0.1 A g-1, the specific capacity recovers to a high-capacity value of 454 mA h g⁻¹.

To further study the electrochemical reaction kinetics of the samples, the EIS tests were performed, and the results are shown in Figure 5e. The resulting Nyquist plots consist of a depressed semicircle in the high-frequency range and a tail in the low-frequency range. In general, the series resistance (R_s) and the charge transfer resistance (R_{ct}) can be extracted from the first point where Z'' = 0 and the diameter of the semicircle, respectively. The slope of the straight line is aligned with the Warburg impendence (Z_w) , which is associated with the diffusion of the lithium ions in the electrode materials.⁶⁹ Compared to the p-MT sample ($R_s = 90 \Omega$), a smaller value of R_s (20 Ω) is observed in the nanohybrids after *n*-Buli treatment, suggesting an improved electrical conductivity of the electrode associated with the higher 1T phase content, which is corresponding to the analysis in Figures 3 and 4. The smaller R_{ct} value and a steeper slope of the straight line in n-MT demonstrate a facile charge transfer process at the electrode/electrolyte interface and a fast ion diffusion process, respectively, which can be attributed to the more dispersed 2D layers and lesser -F-containing functional groups after the n-Buli treatment.

CONCLUSIONS

In summary, we have successfully prepared a 2D MoS₂/Ti₃C₂ composite composed of 1T-phase-enriched MoS2 flakes and functional group-regulated Ti₃C₂ MXene sheets using a bisolvent synthesis method followed by an n-Buli-enabled prelithiation process. Compared with the materials without such treatment, the prelithiated nanohybrids exhibit a distinct surface morphology with higher-1T-metallic phase MoS₂ and lower content of F-based functional groups, which are beneficial for the battery anode performance due to the enhanced electrical conductivity and reduced Li diffusion barrier. As a result, a clearly improved Li-ion storage capacity along with excellent cycle stability is achieved. Our work demonstrates an effective strategy for low-dimensional material structure—property engineering to optimize the battery anode performance. The hybrid structure with high Li-ion storage capacity demonstrated in this study also sheds light on the development of other 2D hybrid-based energy storage and conversion systems.

ASSOCIATED CONTENT

Supporting Information

The Supporting Information is available free of charge at https://pubs.acs.org/doi/10.1021/acsami.2c07984.

Additional SEM and HRTEM images of 2D nanohybrids, EDS results for the F content comparison, SAED patterns and XPS complete survey of p-MT and n-MT, CV curves of the 2D composites, table of LIB anode performance comparison, and rate performance of p-MT and n-MT anodes (PDF)

AUTHOR INFORMATION

Corresponding Authors

Huamin Li — Department of Electrical Engineering, University at Buffalo, The State University of New York, Buffalo, New York 14260, United States; orcid.org/0000-0001-7093-4835; Email: huaminli@buffalo.edu

Fei Yao — Department of Materials Design and Innovation, University at Buffalo, The State University of New York, Buffalo, New York 14260, United States; oocid.org/0000-0001-8414-7955; Email: feiyao@buffalo.edu

Authors

Sichen Wei – Department of Materials Design and Innovation, University at Buffalo, The State University of New York, Buffalo, New York 14260, United States

Yu Fu – Department of Materials Design and Innovation, University at Buffalo, The State University of New York, Buffalo, New York 14260, United States

Pinku Roy – Department of Materials Design and Innovation, University at Buffalo, The State University of New York, Buffalo, New York 14260, United States

Xiao Tong – Center for Functional Nanomaterials, Brookhaven National Laboratory, Upton, New York 11973, United States

Hongyan Yue — School of Materials Science and Engineering, Harbin University of Science and Technology, Harbin 150040, China

Maomao Liu – Department of Electrical Engineering, University at Buffalo, The State University of New York, Buffalo, New York 14260, United States

Hemendra Nath Jaiswal – Department of Electrical Engineering, University at Buffalo, The State University of New York, Buffalo, New York 14260, United States

Simran Shahi – Department of Electrical Engineering, University at Buffalo, The State University of New York, Buffalo, New York 14260, United States

Yannick Iniatius Gata – Department of Materials Design and Innovation, University at Buffalo, The State University of New York, Buffalo, New York 14260, United States Tony Butler – Department of Materials Design and Innovation, University at Buffalo, The State University of New York, Buffalo, New York 14260, United States

Quanxi Jia — Department of Materials Design and Innovation, University at Buffalo, The State University of New York, Buffalo, New York 14260, United States

Complete contact information is available at: https://pubs.acs.org/10.1021/acsami.2c07984

Author Contributions

F.Y. and H.L. conceived and supervised the project. S.W. carried out material synthesis, characterization, and electrochemical tests. Y.F., P.R., T.X., H.Y., M.L, H.J., S.S., Y.I.G., A.B., and Q.J. contributed to material characterization and draft preparation. All authors discussed the results and contributed to the final manuscript.

Notes

The authors declare no competing financial interest.

ACKNOWLEDGMENTS

This work was partially supported by the New York State Energy Research and Development Authority (NYSERDA) under award 138126, the New York State Center of Excellence in Materials Informatics (CMI) under award C160186, and the National Science Foundation (NSF) under award ECCS-1944095. The authors acknowledge support from the Vice President for Research and Economic Development (VPRED) at the University at Buffalo.

REFERENCES

- (1) Tarascon, J.-M.; Armand, M. Issues and Challenges Facing Rechargeable Lithium Batteries. *Nature* **2001**, *414*, 359–367.
- (2) Dunn, B.; Kamath, H.; Tarascon, J.-M. Electrical Energy Storage for the Grid: A Battery of Choices. *Science* **2011**, 334, 928–935.
- (3) Li, M.; Lu, J.; Chen, Z.; Amine, K. 30 Years of Lithium-Ion Batteries. *Adv. Mater.* **2018**, *30*, 1800561.
- (4) Ji, L.; Lin, Z.; Alcoutlabi, M.; Zhang, X. Recent Developments in Nanostructured Anode Materials for Rechargeable Lithium-Ion Batteries. *Energy Environ. Sci.* **2011**, *4*, 2682–2689.
- (5) Nitta, N., Wu, F.; Lee, J. T.; Yushin, G. Li-Ion Battery Materials: Present and Future. *Mater. Today* **2015**, *18*, 252–264.
- (6) Nayak, P. K.; Yang, L.; Brehm, W.; Adelhelm, P. From Lithium-Ion to Sodium-Ion Batteries: Advantages, Challenges, and Surprises. *Angew. Chem., Int. Ed.* **2018**, 57, 102.
- (7) Landi, B. J.; Ganter, M. J.; Cress, C. D.; DiLeo, R. A.; Raffaelle, R. P. Carbon Nanotubes for Lithium Ion Batteries. *Energy Environ. Sci.* **2009**, *2*, 638–654.
- (8) Wu, Z. S.; Ren, W.; Xu, L.; Li, F.; Cheng, H. M. Doped Graphene Sheets as Anode Materials with Superhigh Rate and Large Capacity for Lithium Ion Batteries. *ACS Nano* **2011**, *5*, 5463–5471.
- (9) Qie, L.; Chen, W. M.; Wang, Z. H.; Shao, Q. G.; Li, X.; Yuan, L. X.; Hu, X. L.; Zhang, W. X.; Huang, Y. H. Nitrogen-Doped Porous Carbon Nanofiber Webs as Anodes for Lithium Ion Batteries with a Superhigh Capacity and Rate Capability. *Adv. Mater.* **2012**, 24, 2047—2050.
- (10) Chan, C. K.; Peng, H.; Liu, G.; McIlwrath, K.; Zhang, X. F.; Huggins, R. A.; Cui, Y. High-Performance Lithium Battery Anodes Using Silicon Nanowires. *Nat. Nanotechnol.* **2008**, *3*, 31–35.
- (11) Wu, H.; Cui, Y. Designing Nanostructured Si Anodes for High Energy Lithium Ion Batteries. *Nano Today* **2012**, *7*, 414–429.
- (12) Liu, N.; Wu, H.; McDowell, M. T.; Yao, Y.; Wang, C.; Cui, Y. A Yolk-Shell Design for Stabilized and Scalable Li-Ion Battery Alloy Anodes. *Nano Lett.* **2012**, *12*, 3315–3321.

- (13) Idota, Y.; Kubota, T.; Matsufuji, A.; Maekawa, Y.; Miyasaka, T. Tin-Based Amorphous Oxide: A High-Capacity Lithium-Ion-Storage Material. *Science* **1997**, *276*, 1395–1397.
- (14) Reddy, M. V.; Subba Rao, G. V.; Chowdari, B. V. R. Metal Oxides and Oxysalts as Anode Materials for Li Ion Batteries. *Chem. Rev.* 2013, 113, 5364–5457.
- (15) Wu, Z. S.; Ren, W.; Wen, L.; Gao, L.; Zhao, J.; Chen, Z.; Zhou, G.; Li, F.; Cheng, H. M. Graphene Anchored with Co₃O₄ Nanoparticles as Anode of Lithium Ion Batteries with Enhanced Reversible Capacity and Cyclic Performance. *ACS Nano* **2010**, *4*, 3187–3194.
- (16) Wang, H.; Cui, L. F.; Yang, Y.; Sanchez Casalongue, H.; Robinson, J. T.; Liang, Y.; Cui, Y.; Dai, H. Mn₃O₄-Graphene Hybrid as a High-Capacity Anode Material for Lithium Ion Batteries. *J. Am. Chem. Soc.* **2010**, *132*, 13978–13980.
- (17) Stephenson, T.; Li, Z.; Olsen, B.; Mitlin, D. Lithium Ion Battery Applications of Molybdenum Disulfide (MoS₂) Nanocomposites. *Energy Environ. Sci.* **2014**, *7*, 209–231.
- (18) Chang, K.; Chen, W. L.-Cysteine-Assisted Synthesis of Layered MoS₂/Graphene Composites with Excellent Electrochemical Performances for Lithium Ion Batteries. ACS Nano 2011, 5, 4720–4728.
- (19) Bhandavat, R.; David, L.; Singh, G. Synthesis of Surface-Functionalized WS₂ Nanosheets and Performance as Li-Ion Battery Anodes. *J. Phys. Chem. Lett.* **2012**, *3*, 1523–1530.
- (20) Lukowski, M. A.; Daniel, A. S.; Meng, F.; Forticaux, A.; Li, L.; Jin, S. Enhanced Hydrogen Evolution Catalysis from Chemically Exfoliated Metallic MoS₂ Nanosheets. *J. Am. Chem. Soc.* **2013**, *135*, 10274–10277.
- (21) Acerce, M.; Voiry, D.; Chhowalla, M. Metallic 1T Phase MoS₂ Nanosheets as Supercapacitor Electrode Materials. *Nat. Nanotechnol.* **2015**, *10*, 313–318.
- (22) Wang, S.; Zhang, D.; Li, B.; Zhang, C.; Du, Z.; Yin, H.; Bi, X.; Yang, S. Ultrastable In-Plane 1T-2H MoS₂ Heterostructures for Enhanced Hydrogen Evolution Reaction. *Adv. Energy Mater.* **2018**, *8*, 1801345.
- (23) Yang, S. Z.; Gong, Y.; Manchanda, P.; Zhang, Y. Y.; Ye, G.; Chen, S.; Song, L.; Pantelides, S. T.; Ajayan, P. M.; Chisholm, M. F.; Zhou, W. Rhenium-Doped and Stabilized MoS₂ Atomic Layers with Basal-Plane Catalytic Activity. *Adv. Mater.* **2018**, *30*, 1803477.
- (24) Song, S.; Keum, D. H.; Cho, S.; Perello, D.; Kim, Y.; Lee, Y. H. Room Temperature Semiconductor-Metal Transition of MoTe₂ Thin Films Engineered by Strain. *Nano Lett.* **2016**, *16*, 188–193.
- (25) Wei, S.; Fu, Y.; Liu, M.; Yue, H.; Park, S.; Lee, Y. H.; Li, H.; Yao, F. Dual-Phase MoS₂/MXene/CNT Ternary Nanohybrids for Efficient Electrocatalytic Hydrogen Evolution. *npj* 2D Mater. Appl. 2022. 6, 25.
- (26) Hwang, H.; Kim, H.; Cho, J. MoS2 Nanoplates Consisting of Disordered Graphene-like Layers for High Rate Lithium Battery Anode Materials. *Nano Lett.* **2011**, *11*, 4826–4830.
- (27) Yu, X. Y.; Hu, H.; Wang, Y.; Chen, H.; Lou, X. W. D. Ultrathin MoS₂ Nanosheets Supported on N-Doped Carbon Nanoboxes with Enhanced Lithium Storage and Electrocatalytic Properties. *Angew. Chem., Int. Ed.* **2015**, *54*, 7395–7398.
- (28) Cao, X.; Shi, Y.; Shi, W.; Rui, X.; Yan, Q.; Kong, J.; Zhang, H. Preparation of MoS₂-Coated Three-Dimensional Graphene Networks for High-Performance Anode Material in Lithium-Ion Batteries. *Small* **2013**, *9*, 3433–3438.
- (29) Zhou, J.; Qin, J.; Zhang, X.; Shi, C.; Liu, E.; Li, J.; Zhao, N.; He, C. 2D Space-Confined Synthesis of Few-Layer MoS₂ Anchored on Carbon Nanosheet for Lithium-Ion Battery Anode. ACS Nano 2015, 9, 3837–3848.
- (30) Chang, K.; Chen, W.; Ma, L.; Li, H.; Li, H.; Huang, F.; Xu, Z.; Zhang, Q.; Lee, J. Y. Graphene-like MoS₂/Amorphous Carbon Composites with High Capacity and Excellent Stability as Anode Materials for Lithium Ion Batteries. *J. Mater. Chem.* **2011**, 21, 6251–6257.
- (31) Chang, K.; Geng, D.; Li, X.; Yang, J.; Tang, Y.; Cai, M.; Li, R.; Sun, X. Ultrathin MoS₂ /Nitrogen-Doped Graphene Nanosheets with

- Highly Reversible Lithium Storage. Adv. Energy Mater. 2013, 3, 839–844.
- (32) Teng, Y.; Zhao, H.; Zhang, Z.; Li, Z.; Xia, Q.; Zhang, Y.; Zhao, L.; Du, X.; Du, Z.; Lv, P.; Świerczek, K. MoS₂ Nanosheets Vertically Grown on Graphene Sheets for Lithium-Ion Battery Anodes. *ACS Nano* **2016**, *10*, 8526–8535.
- (33) Zhang, X.; Zhao, R.; Wu, Q.; Li, W.; Shen, C.; Ni, L.; Yan, H.; Diao, G.; Chen, M. Petal-like MoS₂ Nanosheets Space-Confined in Hollow Mesoporous Carbon Spheres for Enhanced Lithium Storage Performance. ACS Nano 2017, 11, 8429–8436.
- (34) Cho, S. H.; Kim, J. H.; Kim, I. G.; Park, J. H.; Jung, J. W.; Kim, H. S.; Kim, I. D. Reduced Graphene-Oxide-Encapsulated MoS₂ /Carbon Nanofiber Composite Electrode for High-Performance Na-Ion Batteries. *Nanomaterials* **2021**, *11*, 2691.
- (35) Song, Q.; Ye, F.; Kong, L.; Shen, Q.; Han, L.; Feng, L.; Yu, G.; Pan, Y.; Li, H. Graphene and MXene Nanomaterials: Toward High-Performance Electromagnetic Wave Absorption in Gigahertz Band Range. *Adv. Funct. Mater.* **2020**, *30*, 2000475.
- (36) Anasori, B.; Lukatskaya, M. R.; Gogotsi, Y. 2D Metal Carbides and Nitrides (MXenes) for Energy Storage. *Nat. Rev. Mater.* **2017**, 2, 16098
- (37) Naguib, M.; Mochalin, V. N.; Barsoum, M. W.; Gogotsi, Y. 25th Anniversary Article: MXenes: A New Family of Two-Dimensional Materials. *Adv. Mater.* **2014**, *26*, 992–1005.
- (38) Attanayake, N. H.; Abeyweera, S. C.; Thenuwara, A. C.; Anasori, B.; Gogotsi, Y.; Sun, Y.; Strongin, D. R. Vertically Aligned MoS_2 on Ti_3C_2 (MXene) as an Improved HER Catalyst. *J. Mater. Chem. A* **2018**, *6*, 16882–16889.
- (39) Hui, X.; Ge, X.; Zhao, R.; Li, Z.; Yin, L. Interface Chemistry on MXene-Based Materials for Enhanced Energy Storage and Conversion Performance. *Adv. Funct. Mater.* **2020**, *30*, 2005190.
- (40) Tang, Q.; Zhou, Z.; Shen, P. Are MXenes Promising Anode Materials for Li Ion Batteries? Computational Studies on Electronic Properties and Li Storage Capability of Ti_3C_2 and $Ti_3C_2X_2$ (X = F, OH) Monolayer. J. Am. Chem. Soc. **2012**, 134, 16909–16916.
- (41) Du, G.; Tao, M.; Gao, W.; Zhang, Y.; Zhan, R.; Bao, S.; Xu, M. Preparation of MoS_2 / $Ti_3C_2T_x$ Composite as Anode Material with Enhanced Sodium/Lithium Storage Performance. *Inorg. Chem. Front.* **2019**, *6*, 117–125.
- (42) Zheng, M.; Guo, R.; Liu, Z.; Wang, B.; Meng, L.; Li, F.; Li, T.; Luo, Y. MoS_2 Intercalated P- Ti_3C_2 Anode Materials with Sandwichlike Three Dimensional Conductive Networks for Lithium-Ion Batteries. *J. Alloys Compd.* **2018**, 735, 1262–1270.
- (43) Shen, C.; Wang, L.; Zhou, A.; Zhang, H.; Chen, Z.; Hu, Q.; Qin, G. MoS₂-Decorated Ti₃C₂ MXene Nanosheet as Anode Material in Lithium-Ion Batteries. *J. Electrochem. Soc.* **2017**, *164*, A2654–A2659
- (44) Alhabeb, M.; Maleski, K.; Anasori, B.; Lelyukh, P.; Clark, L.; Sin, S.; Gogotsi, Y. Guidelines for Synthesis and Processing of Two-Dimensional Titanium Carbide (${\rm Ti_3C_2T_x}$ MXene). *Chem. Mater.* **2017**, 29, 7633–7644.
- (45) Ji, L.; Yan, P.; Zhu, C.; Ma, C.; Wu, W.; Wei, C.; Shen, Y.; Chu, S.; Wang, J.; Du, Y.; Chen, J.; Yang, X.; Xu, Q. One-Pot Synthesis of Porous 1T-Phase MoS₂ Integrated with Single-Atom Cu Doping for Enhancing Electrocatalytic Hydrogen Evolution Reaction. *Appl. Catal., B* **2019**, *251*, 87–93.
- (46) Zhang, Y.; Kuwahara, Y.; Mori, K.; Louis, C.; Yamashita, H. Hybrid Phase 1T/2H-MoS₂ with Controllable 1T Concentration and Its Promoted Hydrogen Evolution Reaction. *Nanoscale* **2020**, *12*, 11908–11915.
- (47) Xiang, T.; Fang, Q.; Xie, H.; Wu, C.; Wang, C.; Zhou, Y.; Liu, D.; Chen, S.; Khalil, A.; Tao, S.; Liu, Q.; Song, L. Vertical 1T-MoS₂ Nanosheets with Expanded Interlayer Spacing Edged on a Graphene Frame for High Rate Lithium-Ion Batteries. *Nanoscale* **2017**, *9*, 6975–6983.
- (48) Ambrosi, A.; Sofer, Z.; Pumera, M. $2H \rightarrow 1T$ Phase Transition and Hydrogen Evolution Activity of MoS₂, MoSe₂, WS₂ and WSe₂ Strongly Depends on the MX₂ Composition. *Chem. Commun.* **2015**, *51*, 8450–8453.

- (49) Dall'Agnese, Y.; Lukatskaya, M. R.; Cook, K. M.; Taberna, P. L.; Gogotsi, Y.; Simon, P. High Capacitance of Surface-Modified 2D Titanium Carbide in Acidic Electrolyte. *Electrochem. Commun.* **2014**, 48, 118–122.
- (50) Wu, M.; Zhan, J.; Wu, K.; Li, Z.; Wang, L.; Geng, B.; Wang, L.; Pan, D. Metallic 1T MoS₂ Nanosheet Arrays Vertically Grown on Activated Carbon Fiber Cloth for Enhanced Li-Ion Storage Performance. *J. Mater. Chem. A* **2017**, *5*, 14061–14069.
- (51) Simon, P. Two-Dimensional MXene with Controlled Interlayer Spacing for Electrochemical Energy Storage. *ACS Nano* **2017**, *11*, 2393–2396.
- (52) Li, H.; Zhang, Q.; Yap, C. C. R.; Tay, B. K.; Edwin, T. H. T.; Olivier, A.; Baillargeat, D. From Bulk to Monolayer MoS₂: Evolution of Raman Scattering. *Adv. Funct. Mater.* **2012**, *22*, 1385–1390.
- (53) Guo, Y.; Zhang, W.; Wu, H.; Han, J.; Zhang, Y.; Lin, S.; Liu, C.; Xu, K.; Qiao, J.; Ji, W.; Chen, Q.; Gao, S.; Zhang, W.; Zhang, X.; Chai, Y. Discovering the Forbidden Raman Modes at the Edges of Layered Materials. *Science* **2018**, *4*, aau6252.
- (54) Lin, Y. C.; Dumcenco, D. O.; Huang, Y. S.; Suenaga, K. Atomic Mechanism of the Semiconducting-to-Metallic Phase Transition in Single-Layered MoS₂. *Nat. Nanotechnol.* **2014**, *9*, 391–396.
- (55) Wang, H.; Lu, Z.; Xu, S.; Kong, D.; Cha, J. J.; Zheng, G.; Hsu, P. C.; Yan, K.; Bradshaw, D.; Prinz, F. B.; Cui, Y. Electrochemical Tuning of Vertically Aligned MoS₂ Nanofilms and Its Application in Improving Hydrogen Evolution Reaction. *Proc. Natl. Acad. Sci. U.S.A.* 2013, 110, 19701–19706.
- (56) Tan, S. J. R.; Abdelwahab, I.; Ding, Z.; Zhao, X.; Yang, T.; Loke, G. Z. J.; Lin, H.; Verzhbitskiy, I.; Poh, S. M.; Xu, H.; Nai, C. T.; Zhou, W.; Eda, G.; Jia, B.; Loh, K. P. Chemical Stabilization of 1T' Phase Transition Metal Dichalcogenides with Giant Optical Kerr Nonlinearity. *J. Am. Chem. Soc.* **2017**, *139*, 2504–2511.
- (57) Wang, F.; Cao, M.; Qin, Y.; Zhu, J.; Wang, L.; Tang, Y. ZnO Nanoparticle-Decorated Two-Dimensional Titanium Carbide with Enhanced Supercapacitive Performance. *RSC Adv.* **2016**, *6*, 88934–88942.
- (58) Tariq, A.; Ali, S. I.; Akinwande, D.; Rizwan, S. Efficient Visible-Light Photocatalysis of 2D-MXene Nanohybrids with Gd₃⁺- and Sn₄⁺- Codoped Bismuth Ferrite. *ACS Omega* **2018**, *3*, 13828–13836.
- (59) Lv, R.; Robinson, J. A.; Schaak, R. E.; Sun, D.; Sun, Y.; Mallouk, T. E.; Terrones, M. Transition Metal Dichalcogenides and beyond: Synthesis, Properties, and Applications of Single- and Few-Layer Nanosheets. *Acc. Chem. Res.* **2015**, *48*, 56–64.
- (60) Dong, Y.; Xu, Y.; Li, W.; Fu, Q.; Wu, M.; Manske, E.; Kröger, J.; Lei, Y. Insights into the Crystallinity of Layer-Structured Transition Metal Dichalcogenides on Potassium Ion Battery Performance: A Case Study of Molybdenum Disulfide. *Small* **2019**, *15*, 1900497.
- (61) Zhu, K.; Wang, X.; Liu, J.; Li, S.; Wang, H.; Yang, L.; Liu, S.; Xie, T. Novel Amorphous MoS₂/MoO₃/Nitrogen-Doped Carbon Composite with Excellent Electrochemical Performance for Lithium Ion Batteries and Sodium Ion Batteries. *ACS Sustainable Chem. Eng.* **2017**, *5*, 8025–8034.
- (62) Come, J.; Black, J. M.; Lukatskaya, M. R.; Naguib, M.; Beidaghi, M.; Rondinone, A. J.; Kalinin, S. V.; Wesolowski, D. J.; Gogotsi, Y.; Balke, N. Controlling the Actuation Properties of MXene Paper Electrodes upon Cation Intercalation. *Nano Energy* **2015**, *17*, 27–35.
- (63) El Ghazaly, A.; Ahmed, H.; Rezk, A. R.; Halim, J.; Persson, P. O. Å.; Yeo, L. Y.; Rosen, J. Ultrafast, One-Step, Salt-Solution-Based Acoustic Synthesis of Ti₃C₂ MXene. *ACS Nano* **2021**, *15*, 4287–4293.
- (64) Li, J.; Yuan, X.; Lin, C.; Yang, Y.; Xu, L.; Du, X.; Xie, J.; Lin, J.; Sun, J. Achieving High Pseudocapacitance of 2D Titanium Carbide (MXene) by Cation Intercalation and Surface Modification. *Adv. Energy Mater.* **2017**, *7*, 1602725.
- (65) Chen, X.; Zhu, Y.; Zhang, M.; Sui, J.; Peng, W.; Li, Y.; Zhang, G. L.; Zhang, F.; Fan, X. N-Butyllithium-Treated Ti₃C₂T_x MXene with Excellent Pseudocapacitor Performance. *ACS Nano* **2019**, *13*, 9449–9456.
- (66) Voiry, D.; Salehi, M.; Silva, R.; Fujita, T.; Chen, M.; Asefa, T.; Shenoy, V. B.; Eda, G.; Chhowalla, M. Conducting MoS₂ Nanosheets

- as Catalysts for Hydrogen Evolution Reaction. *Nano Lett.* **2013**, *13*, 6222–6227.
- (67) Yao, F.; Pham, T.; Lee, H. Carbon-Based Materials for Lithium-Ion Batteries, Electrochemical Capacitors, and Their Hybrid Devices. *ChemSusChem* **2015**, *8*, 2284–2311.
- (68) Wang, Z.; Chen, J. S.; Zhu, T.; Madhavi, S.; Lou, X. W. One-Pot Synthesis of Uniform Carbon-Coated MoO₂ Nanospheres for High-Rate Reversible Lithium Storage. *Chem. Commun.* **2010**, 46, 6906–6908.
- (69) Yao, F.; Güneş, F.; Ta, H. Q.; Lee, S. M.; Chae, S. J.; Sheem, K. Y.; Cojocaru, C. S.; Xie, S. S.; Lee, Y. H. Diffusion Mechanism of Lithium Ion through Basal Plane of Layered Graphene. *J. Am. Chem. Soc.* **2012**, *134*, 8646–8654.